

Imaging with Terahertz Pulses

Timothy Dorney, Jon Johnson, Daniel Mittleman, Richard Baraniuk[†]

Department of Electrical and Computer Engineering, Rice University, Houston, TX 77251-1892, USA

ABSTRACT

Recently, a real-time imaging system based on terahertz (THz) time-domain spectroscopy has been developed. This technique offers a range of unique imaging modalities due to the broad bandwidth, sub-picosecond duration, and phase-sensitive detection of the THz pulses. This paper provides a brief introduction of the state-of-the art in THz imaging. It also focuses on expanding the potential of this new and exciting field through two major efforts. The first concentrates on improving the experimental sensitivity of the system. We are exploring an interferometric arrangement to provide a background-free reflection imaging geometry. The second applies novel digital signal processing algorithms to extract useful information from the THz pulses. The possibility exists to combine spectroscopic characterization and/or identification with pixel-by-pixel imaging. We describe a new parameterization algorithm for both high and low refractive index materials.

Keywords: Terahertz, time-domain spectroscopy, interferometry, parameterization, estimation, refractive index, tomography, spectroscopic imaging

1. INTRODUCTION

Until the 1980's, the use of electromagnetic waves in the far-infrared, or terahertz (THz), region of the spectrum was limited due to the low intensity of thermal sources and the poor sensitivity of most detectors. Many of these difficulties were overcome by the introduction of THz time-domain spectroscopy (THz-TDS).¹⁻³ This system uses femtosecond pulses of near-visible laser light to opto-electronically generate a coherent THz wave. The resulting electromagnetic pulse is broadband and spans from below 100 GHz to more than 2 THz. The receiver structure requires the simultaneous arrival of a delayed femtosecond laser pulse and the generated THz wave. Through this arrangement, the laser pulse acts as a gating signal to control sampling. The result is a system that provides extremely bright, coherent emissions onto a gated receiver with sensitivity several orders of magnitude higher than most bolometric (thermal) counterparts.

The first real-time THz imaging system was introduced in 1995.⁴ In Hu *et al.* and others that followed, a broad range of applications were demonstrated. The images, created from 'T-rays', included moisture analysis in a leaf, thermal analysis of a flame, and leadframe imaging of a plastic encapsulated integrated circuit, just to name a few.⁴⁻⁷ While a broad range of possible applications were presented, the signal processing techniques were often limited in scope. Average received power or arrival time shifts were often used to determine a false color image. This paper focuses on improving the THz system sensitivity through interferometry and generating spectroscopic estimations using digital signal processing.

2. TERAHERTZ TIME-DOMAIN SPECTROSCOPY

The heart of the THz system relies on two key components: the Auston switch and a visible laser capable of generating femtosecond (10^{-15} seconds) pulse trains.¹ The Auston switch is composed of a lithographed dipole antenna patterned on a photoconductive substrate (see Fig. 1). When the dipole antennas are DC biased, a photo-induced current can be generated by the laser pulses. This current rises from zero in a time determined by the duration of each laser pulse, which is typically 0.1 picoseconds. This rapid change in current produces an electromagnetic wave in the THz spectral range.

The receiver optics and switch are similar to the transmitter arrangement just described. The receiver switch, however, is not DC biased. Instead, a current meter is connected across the dipole. Current will only flow when a laser pulse arrives at the

[†] E-mail: tdooney@ieee.org, johnsojl@rice.edu, daniel@rice.edu, richb@rice.edu
Web: www.dsp.rice.edu

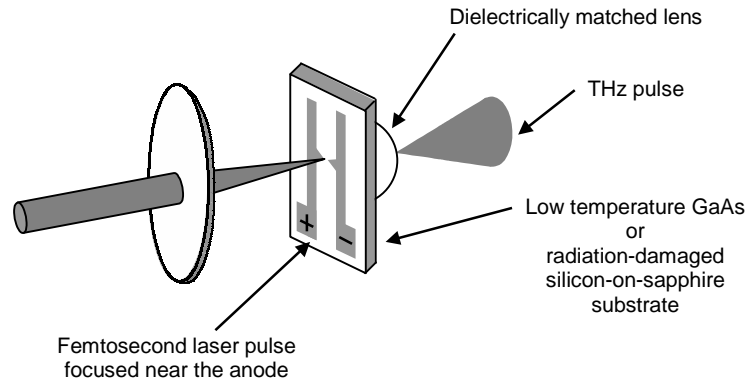


Fig. 1. A THz pulse is generated using an Auston switch. By directing a femtosecond laser pulse onto a DC biased dipole antenna on a semiconductor substrate, a small photo-induced current is created. This current rises from zero in a time determined by the duration of each laser pulse, which is typically 0.1 picoseconds. The rapid change in current produces an electromagnetic wave in the THz spectral range.

switch at the same time as the coherent THz wave. Since the laser pulse is narrow in comparison to the time duration of the T-ray pulse, the laser acts as a gated sampling signal. The optical arrangement between the transmitter and receiver can be tailored depending on the experimental goals.

3. TERAHERTZ INTERFEROMETRY

THz imaging is an emerging technology that permits three-dimensional tomographic imaging of non-metallic objects. Numerous applications have been demonstrated where THz imaging could be a valuable complement to existing technologies for non-invasive testing, including the detection of faults or delaminations in packaged integrated circuits and the location of air bubbles or cracks within polymer or ceramic parts.^{5,6} In many of these applications, the feature we wish to detect is subtle, in the sense that its interaction with the single-cycle THz pulse imposes only a small additional distortion on the waveform. A good example is detecting delamination or disbonding between two surfaces. In many practical cases, the gap which opens between the two surfaces is narrower than the coherence length of the THz pulse, and the waveform is little changed as a result.

Here we report on the use of interferometry in combination with THz tomography, for improving the detectability of such subtle features. This idea has analogies to optical coherence tomography, in which the signal pulse, reflected off of the sample, is interfered with a reference wave to provide enhanced sensitivity.⁸ The experimental layout is shown in Fig. 2. The collimated THz beam is directed into a Michelson interferometer, in which one arm (signal) contains a 10 cm polyethylene lens. Thus, the THz beam is focused onto the sample at normal incidence. The second arm (reference) contains a planar mirror, mounted on a translation stage for variable delay. The measured signal is the coherent superposition of the electric fields from these two arms. Due to the Gouy phase shift acquired by the signal beam as it passes through a focus, it is 180° out of phase from the reference beam.⁹ If the sample reflects the THz pulse without distortion, the delay of the reference arm can be adjusted so that the two pulses destructively interfere at the detector. As a result, we detect almost no signal. Figure 3(a) depicts a waveform in which the sample and reference pulses are separated in time by a few picoseconds. Figure 3(b) shows the waveform when the two pulses are overlapped in time, producing a near cancellation of the measured signal.

Cancellation relies sensitively on the delay and distortions acquired by the signal pulse as it interacts with the sample. Any small change in this waveform produces a large fractional change in the measured signal. We demonstrate the effect of adhesive tape stuck on the cancelled surface. The thickness of this “defect” is approximately 45 μm, or 1/7 of the coherence length of the pulse. The tape is composed of a transparent, low-index polymer, which has only a weak effect on the THz pulse. The waveform in Fig. 3(c) shows the effect of the tape compared to Fig. 3(b). Figure 3(d) shows the minute phase shift between waveforms using conventional (i.e., non-interferometric) imaging. Interferometry enhances the contrast. Figure 4 shows processed images of the tape comparing both an interferometric and non-interferometric arrangement. The

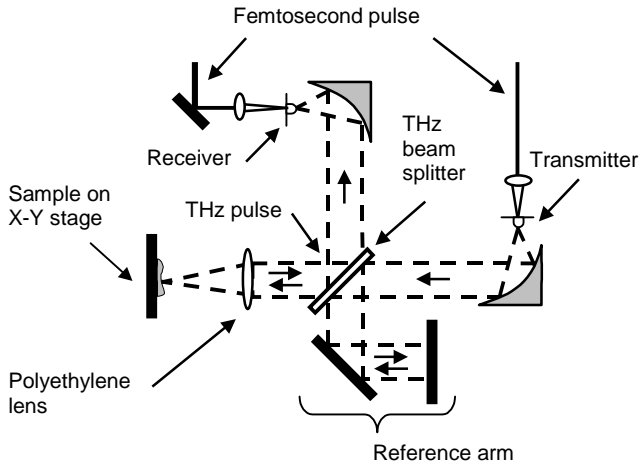


Fig. 2. Schematic of terahertz imaging with interferometry. The reference arm creates an inverted pulse that nearly cancels the main pulse at a known sample depth. Any sample that affects the THz signal disturbs the cancellation with the reference arm. Subtle changes are more easily detected using an interferometric arrangement compared to a non-interferometric setup.

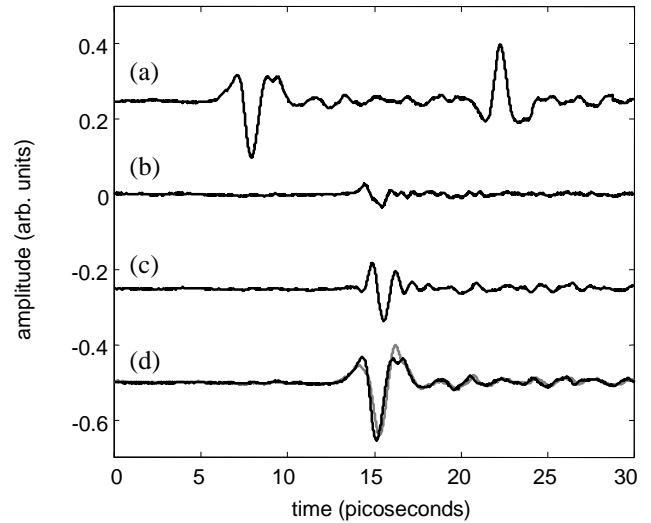


Fig. 3. THz waveforms with (a) a delay between the signal and reference reflections, (b) the near cancellation of the two pulses, (c) the effect on the interferometric signal of the tape, and (d) the effect on the non-interferometric signal of 45 μm thick adhesive tape.

non-interferometric image is barely able to resolve the edges of the tape, while the interferometric image clearly shows the tape and trapped air bubbles under the tape.

4. SPECTROSCOPIC ESTIMATION

One goal in using the THz-TDS system is real-time spectroscopy and imaging. Images are formed by the collection and processing of signals in a pixel-by-pixel fashion as the sample is translated. Issues of particular interest for our purposes are the characterization of the THz waveforms, and the model that describes the interactions between the waveforms and a homogenous, planar solid.

Spectroscopic measurements require an analysis method for THz waveforms. Typically, one measures the transmitted, time-domain waveform both with and without a sample present and then performs a Fourier deconvolution in order to extract material parameters. The success of this method requires precise knowledge of the thickness of the sample, as both the absorption and the phase delay vary exponentially with sample thickness. Indeed, in many of these measurements, the dominant error in the optical constants arises from uncertainty in the thickness measurement. Also, analytical solutions do not exist to derive these constants from the measured electric fields, and we must employ numerical methods.¹⁰ Duvillaret *et al.* recently described one example of a numerical inversion algorithm for this purpose.¹¹ As with most spectroscopic methods, this algorithm also relies on an accurate knowledge of the sample thickness. Very recently, Duvillaret *et al.* extended their work to also extract the thickness, but they only considered high index materials.¹²

In this work, a new technique is proposed to determine simultaneously the thickness and the complex index of refraction of an unknown material.¹² The THz-TDS system provides a time-domain signal that contains not only the initial pulse transmitted through the material but also several subsequent pulses, resulting from internal reflections, which arrive at delayed times. Our method is a model-based approach in which the extraction of material parameters arises from the analysis of the multiple internal reflections described by the Fabry-Perot effect.¹¹ A gradient search minimizes the difference between the model and the measured signals over a range of thicknesses. At each guessed thickness, we iteratively update the complex index of refraction function to minimize the total error. Once the complex index of refraction is identified for a particular thickness, a total variation metric measures the smoothness of the refractive index function. The total variation

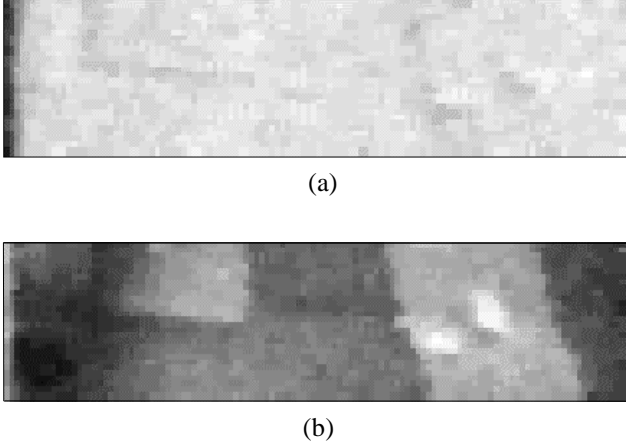


Fig. 4. Images comparing maximum peak-to-peak amplitude of (a) non-interferometric imaging, and (b) interferometric imaging. The sample consists of two $\sim 45\mu\text{m}$ thick pieces of adhesive tape on a flat metal surface. The tape strip on the right has two air bubbles trapped under the tape. Images made from phase variations showed little information for both arrangements.

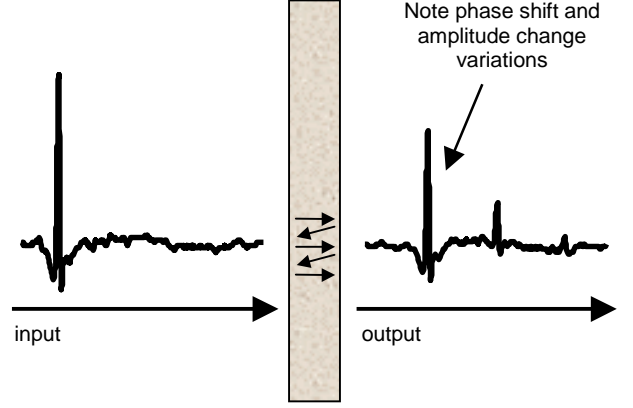


Fig. 5. A terahertz pulse transmitted through a homogeneous, planar material results in the initial pulse, and several subsequent pulses due to multiple internal reflections. These changes, both in the time and frequency domains, form the basis for the information we wish to extract.

metric does not use any simplifying assumptions as in Duvillaret *et al.*¹² The deepest local minimum of the total variation metric as a function of thickness identifies the predicted material thickness and the complex refractive index. We investigate the limits of our method with respect to the minimum measurable refractive index and compare our results to literature data for several different materials.

For each pixel, the system receives a single waveform that is the result of the interactions between the THz pulse and the sample. One may also record a reference waveform without the sample *in situ*. Figure 5 shows a typical THz waveform without sample $E_{\text{ref}}(t)$ characterized by a single-cycle pulse of approximately 1 ps in duration. We also show a waveform measured with a planar sample in the THz path. This waveform $E_{\text{sample}}(t)$ (see Fig. 5 right) shows a similar initial pulse due to the first transmission through the material, but it also contains two smaller pulses caused by multiple internal reflections. The time-domain analog of the Fabry-Perot effect describes these two additional pulses.¹³ We note that all of the pulses in the waveform $E_{\text{sample}}(t)$ are time shifted, attenuated, and reshaped compared to the reference waveform $E_{\text{ref}}(t)$. These changes, both in the time and frequency domains, form the basis for the information we wish to extract. (These experiments were performed in a dry air environment to eliminate the spectral absorption lines due to water vapor.¹⁴)

The Fresnel equations describe the transmission and reflection of the THz wave at each interface.¹³ These are based on the material's complex index of refraction in the frequency domain, $\tilde{n}(\omega) = n(\omega) - j\kappa(\omega)$, where $n(\omega)$ represents the real refractive index, $\kappa(\omega)$ is proportional to the absorption coefficient, and ω is angular frequency. The Fresnel equations at an interface between two layers are:

$$t_{ab}(\omega) = \frac{2\tilde{n}_a(\omega)}{\tilde{n}_a(\omega) + \tilde{n}_b(\omega)}, \quad (1)$$

$$r_{ab}(\omega) = \frac{\tilde{n}_b(\omega) - \tilde{n}_a(\omega)}{\tilde{n}_a(\omega) + \tilde{n}_b(\omega)} \quad (2)$$

where $t_{ab}(\omega)$ is the transmission coefficient of a wave at normal incidence from region a to region b , and $r_{ab}(\omega)$ is the normal reflection in region a at the a - b interface. As the wave moves through a material of thickness l , its propagation is governed by:

$$p_m(\omega, l) = \exp\left(\frac{-j\tilde{n}_m(\omega)\omega l}{c}\right). \quad (3)$$

We neglect scattering (e.g., interface roughness) in our model and consider the THz path both with and without a sample in place. For the free air path, we have:

$$E_{\text{ref}}(\omega) = E_{\text{initial}}(\omega) p_{\text{air}}(\omega, x), \quad \tilde{n}_{\text{air}}(\omega) = 1.00027 - j0 \quad (4)$$

with x the distance between the transmitter and receiver. This includes the small but measurable contribution of the refractive index from air at standard pressure and room temperature.¹⁵ We examine a planar, homogenous material placed in the pathway of the THz radiation. Our iterative approach requires that the primary transmission and at least two multiples be present in the measured waveforms to solve for the free variables. The equations for the primary received signal and two multiples with the sample *in situ* are:

$$E_{\text{primary}}(\omega) = E_{\text{initial}}(\omega) p_{\text{air}}(\omega, (x-l)) t_{01} p_{\text{sample}}(\omega, l) t_{10}, \quad (5)$$

$$\begin{aligned} E_{\text{first multiple}}(\omega) &= E_{\text{initial}}(\omega) p_{\text{air}}(\omega, (x-l)) t_{01} p_{\text{sample}}(\omega, l) r_{10} p_{\text{sample}}(\omega, l) r_{10} p_{\text{sample}}(\omega, l) t_{10} \\ &= E_{\text{initial}}(\omega) p_{\text{air}}(\omega, (x-l)) t_{01} p_{\text{sample}}(\omega, l) t_{10} r_{10}^2 p_{\text{sample}}^2(\omega, l), \end{aligned} \quad (6)$$

$$E_{\text{second multiple}}(\omega) = E_{\text{initial}}(\omega) p_{\text{air}}(\omega, (x-l)) t_{01} p_{\text{sample}}(\omega, l) t_{10} r_{10}^4 p_{\text{sample}}^4(\omega, l). \quad (7)$$

To make our system of equations more tractable, we first add (5) through (7). This models the measured waveform that contains all three temporal signals:

$$E_{\text{complete}}(\omega) = E_{\text{initial}}(\omega) p_{\text{air}}(\omega, (x-l)) t_{01} p_{\text{sample}}(\omega, l) t_{10} \underbrace{\left[1 + \sum_{k=1}^2 \left(r_{10}^2 p_{\text{sample}}^2(\omega, l) \right)^k \right]}_{FP(\omega)}. \quad (8)$$

We are now able to clearly discern the multiples $FP(\omega)$ described by the Fabry-Perot effect. Dividing (8) by (4), we obtain:

$$\hat{H}(\omega) = \frac{E_{\text{complete}}(\omega)}{E_{\text{ref}}(\omega)} = \frac{4\tilde{n}_{\text{air}}(\omega)\tilde{n}_{\text{sample}}(\omega)}{(\tilde{n}_{\text{air}}(\omega) + \tilde{n}_{\text{sample}}(\omega))^2} \left[\exp\left(\frac{-j(\tilde{n}_{\text{sample}}(\omega) - \tilde{n}_{\text{air}}(\omega))\omega l}{c} \right) \right] FP(\omega). \quad (9)$$

Equation (9) provides the transfer function for our model. The complex function $\tilde{n}_{\text{sample}}(\omega)$ and l are the only free variables.

The deconvolution in frequency of our measured temporal signals is:

$$H(\omega) = \frac{E_{\text{sample}}(\omega)}{E_{\text{ref}}(\omega)}. \quad (10)$$

We wish to compare the deconvolution of the measured signals $H(\omega)$ (Eq. 10) with the modeled transfer function $\hat{H}(\omega)$ (Eq. 9). Unfortunately, the real and imaginary parts of $H(\omega)$ are oscillating functions that produce many global minima for any error measure. Instead, using the magnitude and unwrapped phase information provides a unique solution.¹¹ The algorithm must unwrap the phase for both the modeled and measured deconvolution similarly in order to make a valid comparison. In unwrapping, we require that the phase must extrapolate to zero at zero frequency. Our algorithm resets the 0 Hz phase value to zero, and monotonically unwraps all subsequent phases assuming that no two adjacent values have a difference greater than 2π .

We define the error by taking the absolute difference between the magnitude and unwrapped phase of the measured data versus the model:

$$mER(\omega) = |H(\omega)| - |\hat{H}(\omega)|, \quad pER(\omega) = \angle H(\omega) - \angle \hat{H}(\omega). \quad (11)$$

The total error over all frequencies of interest is:

$$ER = \sum_{\omega} |mER(\omega)| + |pER(\omega)|. \quad (12)$$

Duvillaret *et al.* used a somewhat different error calculation by taking the squared error of the natural log of the magnitude, and the unwrapped phase.¹¹ Since we do not apply a parabolic fit method to match the model to the measured signals, we do not use the same error measure.

Our procedure uses a three step process. First, we make an initial guess at the thickness. Second, our algorithm calculates the beginning functions for the complex index of refraction. The initial guess assumes a non-dispersive material. Third, a gradient descent algorithm iterates the complex index of refraction function in frequency until the total error no longer monotonically decreases. Our algorithm records the final complex refractive index function, and repeats these steps for a range of thicknesses. We review each of these steps in detail below.

First, the algorithm bounds the upper and lower limits of thickness guesses by:

$$l_{\text{upper}} = \frac{\Delta t c}{n_1 - n_{\text{air}}}; \quad l_{\text{lower}} = \frac{\Delta t c}{n_2 - n_{\text{air}}} \quad (13)$$

where Δt is the time delay between the pulse in $E_{\text{ref}}(t)$ and the first pulse in $E_{\text{sample}}(t)$ of the measured signals. The parameters n_1 and n_2 limit the range of refractive indices considered. Values of $n_1 = 1.2$ and $n_2 = 8$ cover nearly all practical cases.

Second, the best initial starting function for the complex refractive index occurs when the first peak location of the temporal model's deconvolution is the same as the first peak location of the measured deconvolution. The real refractive index and the thickness of a material control where the first peak exists in the temporal deconvolution. The imaginary index of refraction and the thickness affect the amplitude of the first peak. Assuming a non-dispersive material (flat frequency response) for the estimated $n(\omega)$, the following equation governs the relationship between the thickness and real refractive index based on the location of the pulse in the measured signal's temporal deconvolution:

$$n = \left(\frac{\text{argmax}(|h(t)|) c}{l} \right) + 1.00027 \quad (14)$$

where l is the estimated thickness of the material selected in the first step and $\text{argmax}(|h(t)|)$ is the time index of the absolute maximum of the measured temporal deconvolution. This assumes that the input signal begins at $t = 0$. We do not expect a constant real refractive index in most real materials, but this provides a good way to generate an initial estimate. The initial value for $\kappa(\omega)$ begins at zero and increments until the absolute maximum of the modeled temporal deconvolution is less than or equal the absolute maximum of the measured temporal deconvolution.

Third, after the initialization of $n(\omega)$ and $\kappa(\omega)$, they are updated using a gradient descent algorithm:¹⁶

$$n_{\text{new}}(\omega) = n_{\text{old}}(\omega) + \varepsilon pER(\omega), \quad \kappa_{\text{new}}(\omega) = \kappa_{\text{old}}(\omega) + \varepsilon mER(\omega) \quad (15)$$

where ε is the update step size. It determines how much of an effect the magnitude and phase error has on the new values for the complex refractive index. (A reasonable value is $\varepsilon = 0.01$.) The algorithm updates the complex index of refraction functions until the total error in (12) is no longer monotonically decreasing. Unlike Duvillaret *et al.*, we do not place any assumptions on $\kappa(\omega)$ for the model.¹²

Our algorithm applies the three steps outlined above to generate a complex index of refraction function for a variety of guessed thicknesses. Figure 5 shows the final error obtained from our gradient descent algorithm at a variety of different guessed thicknesses for a sample of silicon. The shape of the plot is typical. The decaying exponential trend for small thicknesses is due to the exponential bias created by (9) for the model. The growing exponential trend for large thicknesses is an artifact of the update step size in the gradient descent algorithm. A smaller update coefficient (ε) would maintain the error curve near zero but dramatically increase the computational load. Under simulation, a global minimum is observed; however, experimentally obtained data, at best, provides a deepest *local* minimum. If the material under investigation has a relatively small real index of refraction, the concave error surface surrounding this minimum is extremely narrow. Typical step sizes for thickness easily skip this local minimum; therefore, selection of the deepest local minimum for some samples is problematic. We require a metric to identify which thickness and complex refractive index pair are the predicted properties for our sample. Instead of using total error, we introduce the total variation of degree one:^{17,18}

$$D[m] = |n[m-1] - n[m]| + |\kappa[m-1] - \kappa[m]|, \quad TV = \sum D[m] \quad (16)$$

where the complex index of refraction is $\tilde{n}(\omega) = n(\omega) - j\kappa(\omega)$ and the sum ranges over the useful data, between 250 GHz and 2 THz.

Total variation measures the smoothness of the refractive index at the minimum identified by the gradient descent algorithm for each thickness. The deepest local minimum for TV is more easily determined than the deepest local minimum for total

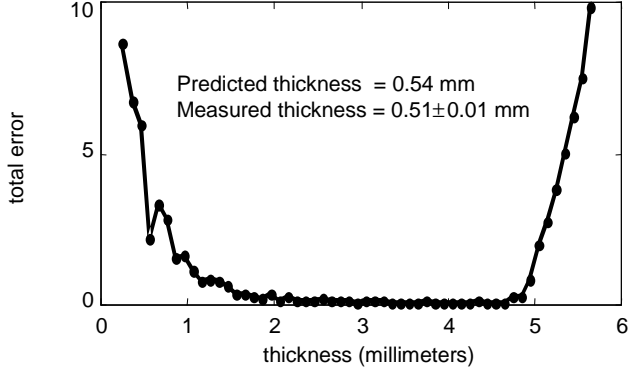


Fig. 5. The total error between the model and measured signals for a 0.51 mm thick sample of silicon plotted over a wide range of thicknesses.

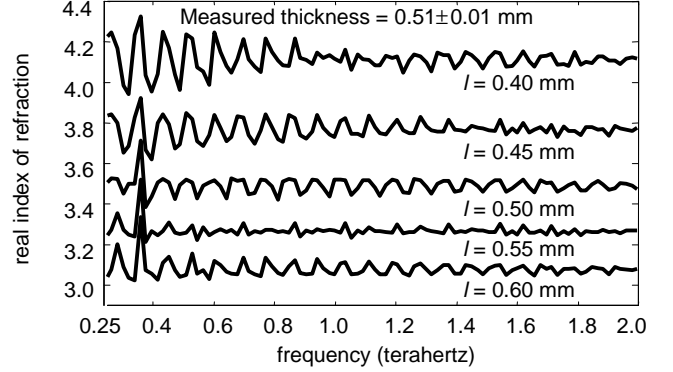


Fig. 6. Final real index of refraction obtained from our algorithm at various guessed thicknesses. As we approach the appropriate thickness, the oscillations in the complex index of refraction decrease. The general trend as the guessed thickness increases, however, is the decrease in amplitude for the complex refractive index. This leads us to use the deepest *local* minimum and the total variation of degree one metric in (16) and (17).

error because the *TV* error surface provides a very broad concave region around the deepest local minimum. For most samples, we do not expect that the recorded complex index of refraction varies dramatically from one frequency sample to the next, since the sampled frequency step size is relatively small. (Our temporal window width is approximately 50 ps with a sample rate of 5 fs, which gives a frequency sampling of $\Delta f = 20$ GHz.) Though the index may have strong variations with frequency, the majority of solid materials do not have sharp spectral features compared to Δf .^{3,19} Note that this method fails for samples with sharp spectral features (e.g., gases).

At each thickness, we use the recorded complex index of refraction at the final total error to calculate the total variation. As shown in Fig. 6, the complex index of refraction shows a marked reduction in oscillations at the proper thickness. We observe, however, that the amount of ripple in $n(\omega)$ and $\kappa(\omega)$ also decreases as l increases. By identifying the thickness at which the deepest *local* minimum for total variation occurs, our algorithm identifies the proper thickness.

Due to the large range of thicknesses to be considered, we apply the three steps outlined above on three different thickness ranges and stepping distances. The first pass uses a coarse stepping distance over the full range of thicknesses identified in (13). The next two passes use finer stepping distances over a limited range identified from the previous pass. The deepest local minimum of the total variation on each pass determines the center point for the next finer pass. In a limited number of simulations, the final pass did not contain a minimum; therefore, we modified the total variation metric:

$$TV2 = \sum |D[m] - D[m+1]|. \quad (17)$$

This modified total variation takes the absolute difference between adjacent points of (16). Using (17), we are able to amplify the variations in the smoothness measure.

5. RESULTS FOR HIGH REFRACTIVE INDEX MATERIALS

We examine several high index materials and investigate the general limits of this method. Our method requires that the primary transmission pulse and two multiples are identified in the signal. Materials with low refractive indices may not have enough multiples above the signal-to-noise (SNR) floor. We present the silicon wafer data that was already introduced, and look at two other high index materials, GaAs and LiNbO₃ (ordinary axis).

We first consider the data for the silicon wafer sample. Previous THz-TDS studies used silicon as a sample material since it has essentially zero absorption and a flat spectral response (i.e., $\tilde{n}(\omega) = 3.42 - j 0$).^{11,12,19} Figure 5 shows the total error plotted over the initial coarse sampling of thicknesses for a high resistivity silicon wafer sample ($\rho > 10^4 \Omega \text{ cm}$).

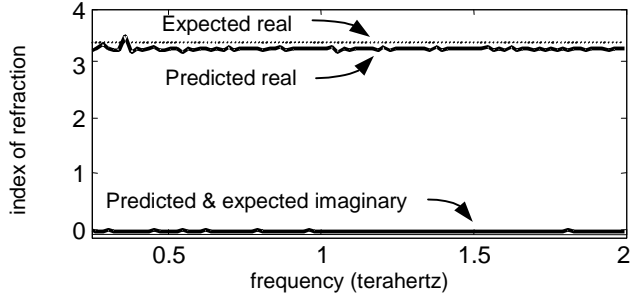


Fig. 7. The real and imaginary index of refraction for the predicted thickness identified in Fig. 5. Literature data puts the complex index of refraction of silicon at $3.418 - j0$.

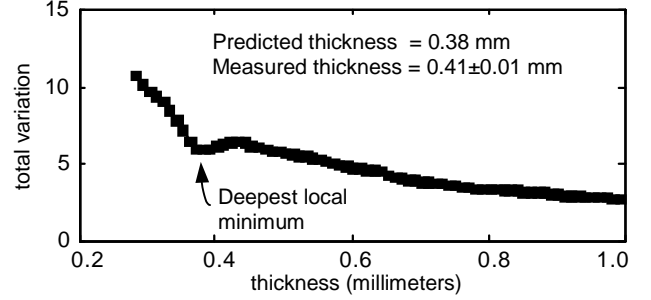


Fig. 8. The total variation (TV) measure for GaAs is shown with a 0.01 mm stepping distance for thickness. Each thickness step is indicated by a square marker which creates a thick line. The deepest local minimum is easily identified.

Measurements made with calipers put the expected thickness at approximately 0.51 ± 0.01 mm. The deepest local minimum identified in Fig. 5 is approximately $30 \mu\text{m}$ from the measured value. The predicted thickness error is ten times less than the coherence length of the terahertz pulse. Figure 7 contains the real and imaginary index of refraction results at the thickness (0.54 mm) identified from the $TV2$ metric in (17). The solid lines indicate the predicted values. The dashed line at 3.42 is the expected real refractive index from the literature.¹⁹ The predicted and expected values for the imaginary component are superimposed. The real index is slightly low, since the predicted thickness is slightly high; however, both the real and imaginary predicted values are independent of frequency as expected. The primary source of error occurs due to alignment since it is difficult to guarantee that the sample is normal to the propagation direction of the THz beam.

A second sample, semi-insulating GaAs, has the following expected complex index of refraction:²⁰

$$\tilde{n}(\omega) = \sqrt{11 \left(1 + \frac{11.794}{8.055^2 - \nu^2 + j0.0719\nu} \right)} \quad (18)$$

where ν is frequency in THz. Due to greater manufacturing variations, the complex index of refraction of GaAs varies more from sample to sample, so (18) is at best an approximate expression. Figure 8 shows the total variation over a range of thicknesses. The predicted thickness for GaAs is 0.38 mm compared to the measured thicknesses of 0.41 ± 0.01 mm. The initial stepping distance used to identify a local minimum is 0.01 mm. In Fig. 9, we show the real index of refraction at the predicted and measured thicknesses for GaAs. The dashed line represents the expected values from the literature.²⁰ We also plot the real index of refraction at the measured thickness for comparison. A small variation in the predicted thickness corresponds to a slight difference in the real index. Third, we examine LiNbO_3 (ordinary axis). The predicted thickness is 0.44 mm, and the measured thickness is 0.50 ± 0.02 mm. We show the real index of refraction in Fig. 10. The dashed line in Fig. 10 represents the literature data for LiNbO_3 .²⁰ The range of the real indices between these three samples is dramatic.

Since the technique requires that the primary and two multiples be present in the measured waveforms, it is difficult to obtain the parameters from materials with low indices of refraction. To explore this limit, we turn to simulation. To validate our approach at low values of refractive index, we create a simulated system to produce both the input and output time domain waveforms. A Rayleigh distribution models the faster current rise and slower current fall in a photoconductive switch. We modify the distribution to smooth the region around the origin so that it is differentiable. The derivative of the modified Rayleigh distribution is used as the model for a single-cycle THz pulse.

From SNR measurements of the THz system, we reasonably expect a ratio of 1,500:1 using a relatively large number of averaged waveforms (>500). Using simulations and a captured noise signature, we determine the minimum real index resolved by our algorithm. Figure 11 shows the range of parameters for which the method is applicable. The circles indicate test cases that passed using the thicknesses indicated by the vertical dashed lines and using a constant frequency, real index of refraction. The imaginary index is assumed zero in these simulations. The shaded area represents the region where the test cases passed. Below this region, the method is limited by SNR. Above this region, we expected the simulations to pass. The initial step size, however, was too large to produce a local minimum, or the analysis window size (25 ps in this simulation) limited the number of multiples. Obviously, both the thickness stepping size and analysis window can be changed depending on the material under investigation. For example in Fig. 10, the thickness stepping size was modified to

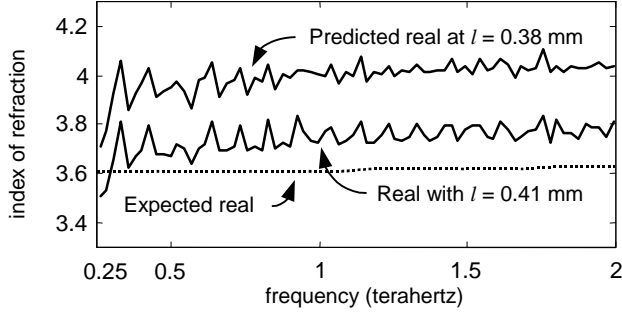


Fig. 9. The real refractive index for the predicted and measured thickness, and the real index from the literature are displayed for a sample of GaAs. Manufacturing variations are more common for GaAs compared to silicon.

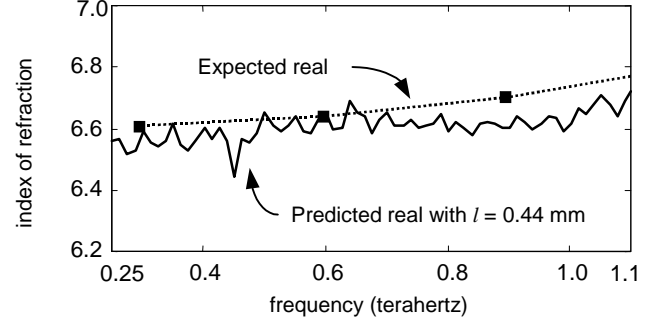


Fig. 10. The predicted real refractive index and the real index from the literature are displayed for a sample of LiNbO_3 (ordinary axis).

account for the larger index. Consequently, the region of applicability in Fig. 11 is only bounded below. For a given SNR ratio, there is a corresponding limit to the minimum real refractive index that can be studied. The next section addresses this issue.

6. LOW INDEX MATERIAL PARAMETERIZATION

In the previous section, the signal-to-noise ratio limited the ability to investigate low real index of refraction materials. We require the primary and two multiple reflections to use the method above; however, sufficient information is obtained through an alternative methodology. By collecting at least three or more transmission waveforms with the sample at different angles of incidence, the different optical pathways provide sufficient information. Obviously, this method also works with high index materials.

In Fig. 12, a terahertz pulse is incident on the sample at an angle α . Since the angle is not necessarily perpendicular to the sample, we redefine Fresnel's transmission coefficient from (1) with (19):

$$t_{ab}(\omega) = \frac{2\tilde{n}_a(\omega)\cos\alpha}{\tilde{n}_a(\omega)\cos\beta + \tilde{n}_b(\omega)\cos\alpha}, \quad (19)$$

where α is known and β is defined by Snell's law:¹³

$$\beta = \arcsin\left(\frac{n_a \sin\alpha}{n_b}\right). \quad (20)$$

The propagation coefficient through the sample is no longer dependent on the thickness l , but instead, it is dependent on r :

$$r = \frac{l}{\cos\beta}. \quad (21)$$

We must also determine the propagation distance of the terahertz pulse in air with the sample *in situ*. This distance between the transmitter and receiver, minus the path through the material, depends on the rotation angle of the sample and how much the incident pulse is refracted. The amount subtracted from the distance between the emitter and detector is defined as the following:

$$m = r \cos(\alpha - \beta), \text{ where } \alpha \geq \beta. \quad (22)$$

Using a similar set of arguments as in Section 4, we rewrite (5) as (23):

$$E_{\text{transmitted}}(\omega) = E_{\text{initial}}(\omega) p_{\text{air}}(\omega, (x-m)) t_{01} p_{\text{sample}}(\omega, r) t_{10}. \quad (23)$$

The deconvolution is obtained by dividing (23) by (4):

$$\hat{H}(\omega) = \frac{E_{\text{transmitted}}(\omega)}{E_{\text{ref}}(\omega)} = \frac{4\tilde{n}_{\text{air}}(\omega)\tilde{n}_{\text{sample}}(\omega)\cos\alpha\cos\beta}{(\tilde{n}_{\text{air}}(\omega)\cos\beta + \tilde{n}_{\text{sample}}(\omega)\cos\alpha)^2} \left[\exp\left(\frac{-j(r\tilde{n}_{\text{sample}}(\omega) - m\tilde{n}_{\text{air}}(\omega))\omega}{c}\right) \right]. \quad (24)$$

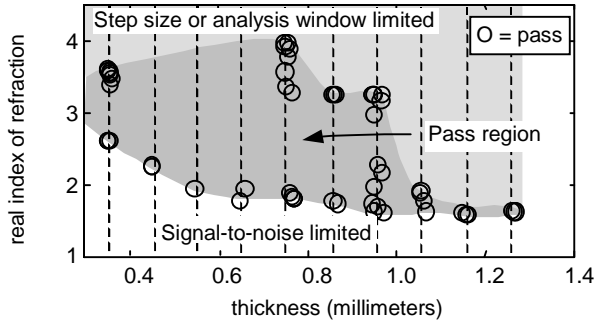


Fig. 11. The limits of our method displayed for a simulated material at a signal-to-noise of 1500:1. The circles indicate the test cases that passed for the thickness indicated by the vertical dashed lines. At each point, the real refractive index was constant across frequency while the imaginary component was zero. The solid area represents the passing region. The area below the passing region is signal-to-noise limited. The light gray area at the top indicates a region that should pass; however, the initial stepping distance for thickness needs to be smaller and/or the data record needs to be longer. At larger thicknesses or higher real index, the multiple reflections might exceed the data record limits.

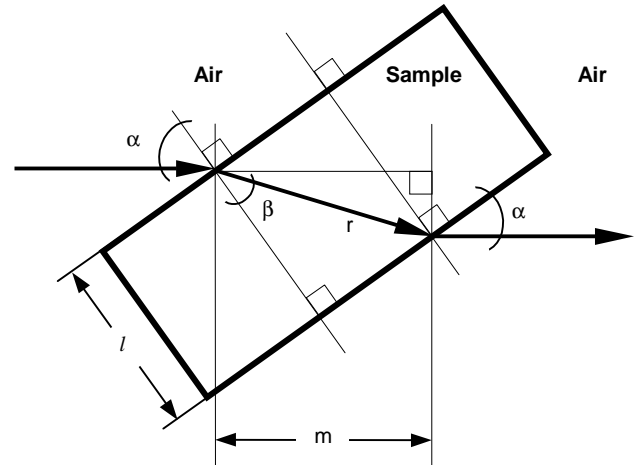


Fig. 12. The method to parameterize high real index materials is dependent on a primary transmission pulse and two multiple reflections. Low real index materials do not produce multiples above the signal-to-noise ratio. To compensate, we use different optical path lengths, obtained by rotating the sample through different angles, to provide sufficient information to estimate the material's parameters.

Equation (24) provides the transfer function for our model, and the complex function $\tilde{n}_{\text{sample}}(\omega)$ and l are the only free variables.

To determine the proper solutions for the free variables, we follow the same process outlined for the high index materials. To recap, the following five steps are used:

1. Guess a thickness.
2. Generate an initial estimate for the complex refractive index assuming a non-dispersive material.
3. Use a gradient descent algorithm to adjust the complex refractive index to minimize the absolute difference error.
4. Record the total variation of the 1st degree.
5. Repeat steps 1-4 for a range of thicknesses.

The final step is different from the previously described procedure in Section 4. Instead of the deepest local minimum, a global minimum determines the solution. This follows the traditional procedure used in tomography.

7. RESULTS FOR LOW INDEX MATERIALS

Due to the ease of use and precision provided by an electro-mechanical rotational stage, we recorded eleven terahertz waveforms and one reference for a sample. The incidence angles ranged from 0° to 50° in 5° increments. Even though the range and spacing of the angles were highly controlled, the initial angle, normal to the sample, was subject to error.

Unfortunately, the recorded waveforms are dependent on the initial angle; therefore, this information can not be determined using only the data. An initial angle error causes the phase delay to be increased for all of the results. In turn, the material thickness appears larger than the actual, and subsequently, the real index is lower than expected. We, therefore, use a known sample to calibrate the experiments. As before, silicon provides a good starting point for our investigation. Since the complex index of refraction is known, we used silicon to iteratively determine an offset angle that is incorporated into the algorithm for all other materials. The offset is fixed when the mean of the real refractive index approximates 3.42, regardless of the predicted thickness. In this work, an offset of -1.15° was determined.

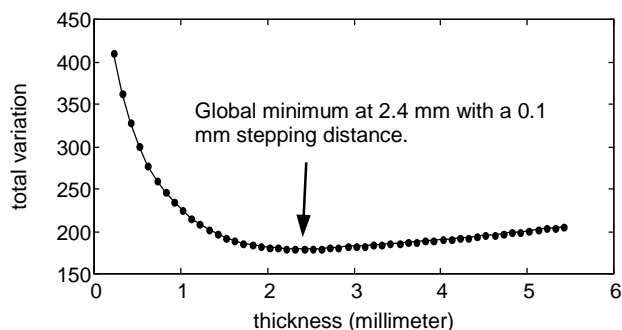


Fig. 13. The total variation measure for teflon shown with a 0.1 mm stepping distance. With this algorithm, the global minimum, and not the deepest local minimum, determines the proper thickness.

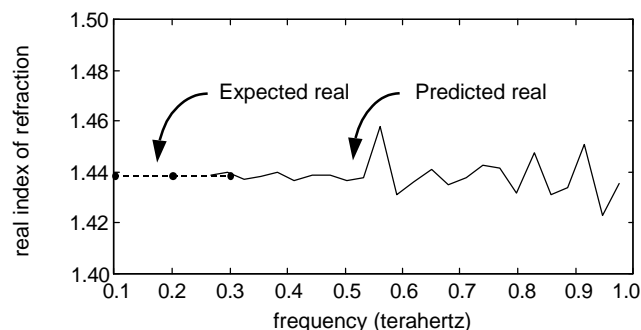


Fig. 14. The real refractive index for the predicted thickness of 2.458 mm compared to the index from the literature. The measured thickness was approximately 2.466 ± 0.03 mm. The mean of the predicted real index is the same as the expected value.

A sample of teflon was used for this investigation. The measured thickness was approximately 2.466 ± 0.03 mm. The predicted thickness was 2.458 mm. Figure 13 shows the total variation error curve. Again note that we search for the global minimum and not the deepest local minimum in the case. Figure 14 displays the resulting real index of refraction. Interestingly, the mean of the predicted real refractive index is 1.438. This is the value quoted in the literature.²¹

8. SUMMARY

We have briefly explained the opto-electronic mechanisms that allow THz emission and detection. By introducing an interferometric arrangement, the sensitivity of the system is improved. We demonstrate qualitative assessment with an image of tape that has a thickness 1/7 of the coherence length of the terahertz pulse. A non-interferometric arrangement barely resolves the tape, whereas the interferometric method clearly shows the tape and trapped air bubbles. Next, we introduced a spectroscopic imaging method that simultaneously and independently determines the complex index of refraction and thickness of a sample. We extend this method to allow the same parameters to be obtained from low index material by using multiple waveforms. Results from both methods are provided which demonstrate very good performance. Thickness measurements have an error much smaller than the coherence length of our THz source. The index of refraction results match both the value and dispersion characteristics recorded in the literature.

ACKNOWLEDGEMENTS

We wish to acknowledge the support of the Army Research Office, the Environmental Protection Agency, and the National Science Foundation. We also acknowledge the efforts of Joel Boyd and Ashvin George to maintain and automate the laboratory. Further information is available at www.dsp.rice.edu/~mit.

REFERENCES

1. P. Smith, D. Auston, and M. Nuss, "Subpicosecond Photoconducting Dipole Antennas," *IEEE J. Quant. Elec.*, **24**(2), 255-260 (1988).
2. M. van Exter and D. Grischkowsky, "Characterization of an Optoelectronic Terahertz Beam System," *IEEE Trans. Micro. Theo. Tech.*, **38**, 1684-1691 (1990).
3. M. Nuss and J. Orenstein, "Terahertz Time-Domain Spectroscopy (THz-TDS)," in *Millimeter and Submillimeter Wave Spectroscopy of Solids*, ed. G. Grüner, (Heidelberg, Germany: Springer-Verlag, 1998), and references therein.
4. B. Hu and M. Nuss, "Imaging with terahertz waves," *Opt. Lett.*, **20**(16), 1716-1718 (1995).
5. D. Mittleman, R. Jacobsen, and M. Nuss, "T-ray imaging," *IEEE J. Sel. Top. Quant. Elect.*, **2**(3), 679-692 (1996).
6. D. Mittleman, S. Hunsche, L. Boivin, and M. Nuss, "T-ray tomography," *Opt. Lett.*, **22**(12), 904-906 (1997).
7. D. Mittleman, M. Gupta, R. Neelamani, R. Baraniuk, J. Rudd, and M. Koch, "Recent advances in terahertz imaging," *Appl. Phys. B*, **68**, 1085-1094 (1999).

8. D. Huang, E. Swanson, C. Lin, J. Schuman, W. Stinson, W. Chang, M. Hee, T. Flotte, K. Gregory, C. Puliafito, and J. Fujimoto, "Optical coherence tomography," *Science*, **254**, 1178-1181 (1991).
9. A. Ruffin, J. Rudd, J. Whitaker, S. Feng, and H. Winful, "Direct observation of the Gouy phase shift with single-cycle terahertz pulses," *Phys. Rev. Lett.*, **83**(17), 3410-3413 (1999).
10. D. Colton and R. Kress, *Inverse Acoustic and Electromagnetic Scattering Theory*, 2nd ed. (Heidelberg, Germany: Springer-Verlag, 1998), 2-7.
11. L. Duvillaret, F. Garet, and J. Coutaz, "A Reliable Method for Extraction of Material Parameters in Terahertz Time-Domain Spectroscopy," *IEEE J. Sel. Top. Quant. Elec.*, **2**, 739-746 (1996).
12. L. Duvillaret, F. Garet, and J. Coutaz, "Highly Precise Determination of Both Optical Constants and Sample Thickness in Terahertz Time-Domain Spectroscopy," *Appl. Opt.*, **38**, 409-415 (1999).
13. E. Hecht, *Optics*, 2nd ed. (Reading, Massachusetts: Addison-Wesley, 1987).
14. M. van Exter, C. Fattinger, and D. Grischkowsky, "TeraHertz time-domain spectroscopy of water vapor," *Opt. Lett.*, **14**, 1128 (1989).
15. P.E. Ciddar, "Refractive index of air: new equations for the visible and near infrared," *Appl. Opt.*, **35**, 1566-1573 (1996).
16. S. Haykin, *Adaptive Filter Theory*, (Englewood Cliffs, New Jersey: Prentice Hall, 1996).
17. J.E. Odegard and C.S. Burrus, "Discrete finite variation: a new measure of smoothness for the design of wavelet basis," *Proc. of ICASSP*, 1467-1470 (1996).
18. F. Jones, *Lebesgue Integration on Euclidean Space*, (Boston, MA: Jones and Bartlett, 1993).
19. D. Grischkowsky, S. Keiding, M. van Exter, and C. Fattinger, "Far-infrared time-domain spectroscopy with terahertz beams of dielectrics and semiconductors," *J. Opt. Soc. Am. B*, **7**, 2006-2015 (1990).
20. E.D. Palik, *Handbook of Optical Constants of Solids*, (Academic Press, 1985).
21. M.N. Afsar, "Precision Millimeter-Wave Measurement of Complex Refractive Index, Complex Dielectric Permittivity, and Loss Tangent of Common Polymers," *IEEE Trans. Instr. and Meas.*, **IM-36**, 530-536 (1987).